Earth and Planetary Science Letters 540 (2020) 116269

Contents lists available at ScienceDirect

Earth and Planetary Science Letters

www.elsevier.com/locate/epsl

Mysterious tsunami in the Caribbean Sea following the 2010 Haiti earthquake possibly generated by dynamically triggered early aftershocks

Uri ten Brink [a], Yong Wei [b,c], Wenyuan Fan [d], Jose-Luis Granja-Bruña [e], Nathan Miller [a]

[a] USGS, Woods Hole, MA 02543, USA
[b] JISAO, University of Washington, WA 98105, USA
[c] NOAA-PMEL, Seattle, WA 98115, USA
[d] Florida State University, Tallahassee, FL 32306, USA
[e] Universidad Complutense de Madrid, Madrid, Spain

ARTICLE INFO

Article history:
Received 27 September 2019
Received in revised form 3 April 2020
Accepted 5 April 2020
Available online xxxx
Editor: M. Ishii

Keywords:
dynamically-triggered aftershocks
instantaneous aftershocks
tsunami warning protocol
DART buoy
tsunami from land-based earthquake
tsunami from strike-slip earthquake

ABSTRACT

Dynamically triggered offshore aftershocks, caused by passing seismic waves from main shocks located on land, are currently not considered in tsunami warnings. The M7.0 2010 Haiti earthquake epicenter was located on land 27 km north of the Caribbean Sea and its focal mechanism was oblique strike-slip. Nevertheless, a tsunami recorded on a Caribbean Deep-Ocean Assessment and Reporting of Tsunami (DART) buoy and a tide gauge produced runup heights of 1–3 m along Haiti southeast coast. Earthquake finite-fault model inversions of the DART waveform suggest that a reverse fault doublet with magnitudes of M6.8 and M6.5 located 85 km southwest of the epicenter may have excited the tsunami. This doublet collocates with dynamically triggered aftershocks, derived from back-projection analysis, that occurred 20-60 s after the main shock of the Haiti earthquake. The aftershocks are within a region of maximum dynamic strain predicted by the main shock, on a possibly tectonically active submarine ridge southwest of Haiti's Southern Peninsula. The agreement between the tsunami finite-fault source models and the seismic and tectonic evidence suggests that earthquakes on land, even strike-slip faults, can generate tsunamis by dynamically triggering offshore aftershocks.

Published by Elsevier B.V.

1. Introduction

The M7.0 2010 Haiti earthquake along the Enriquillo Fault west of Port-Au-Prince, Haiti, ruptured a complex fault network including both strike-slip and reverse faults (Hayes et al., 2010). The ruptured fault network was less than 60 km long, spanning from the northern side of Haiti's Southern Peninsula on land to the north of the peninsula offshore (Fig. 1). The offshore rupture produced a minor tsunami that impacted the north shore of the peninsula (Hornbach et al., 2010; Fritz et al., 2013). Intriguingly, a much more prominent tsunami was reported along the south shore of the peninsula, in the Caribbean Sea, with 3 m runup in Jacmel and 1 to 2 m runups as far east as Pedernales on the Dominican Republic border (Fritz et al., 2013). The static Coulomb stress change from the 2010 Haiti earthquake mainshock can explain the majority of observed aftershocks, which are located west and east of the mainshock along the northern part of the peninsula and along offshore faults north of the peninsula (Symithe et al., 2013). In contrast, there is a paucity of aftershocks along the south shore of the peninsula (Douilly et al., 2013).

Fritz et al. (2013) modeled the tsunami south of the island with mainshock source parameters close to the parameters provided by the global CMT solution (http://www.globalcmt.org/) but with two crucial differences. The Fritz et al. (2013) model required a uniform 5.8 m slip model, yielding a total moment magnitude of 7.47, whereas the moment magnitude of the earthquake was 7.0 (https://earthquake.usgs.gov/earthquakes/eventpage/usp000h60h/). In addition, the modeled fault dipped southward, whereas both the CMT solution and the interferometric synthetic-aperture radar (InSAR) inversion (Hayes et al., 2010) suggested a north-dipping fault. Consequently, the Fritz et al. (2013) source model would predict a broad co-seismic uplift reaching the south coast, which was not observed in the InSAR data (Hayes et al., 2010; Symithe et al., 2013).

We propose that near-instantaneous dynamically-triggered aftershocks located in the Caribbean Sea ~85 km southwest of the mainshock epicenter generated the tsunami south of the island.

E-mail address: utenbrink@usgs.gov (U. ten Brink).

https://doi.org/10.1016/j.epsl.2020.116269
0012-821X/Published by Elsevier B.V.

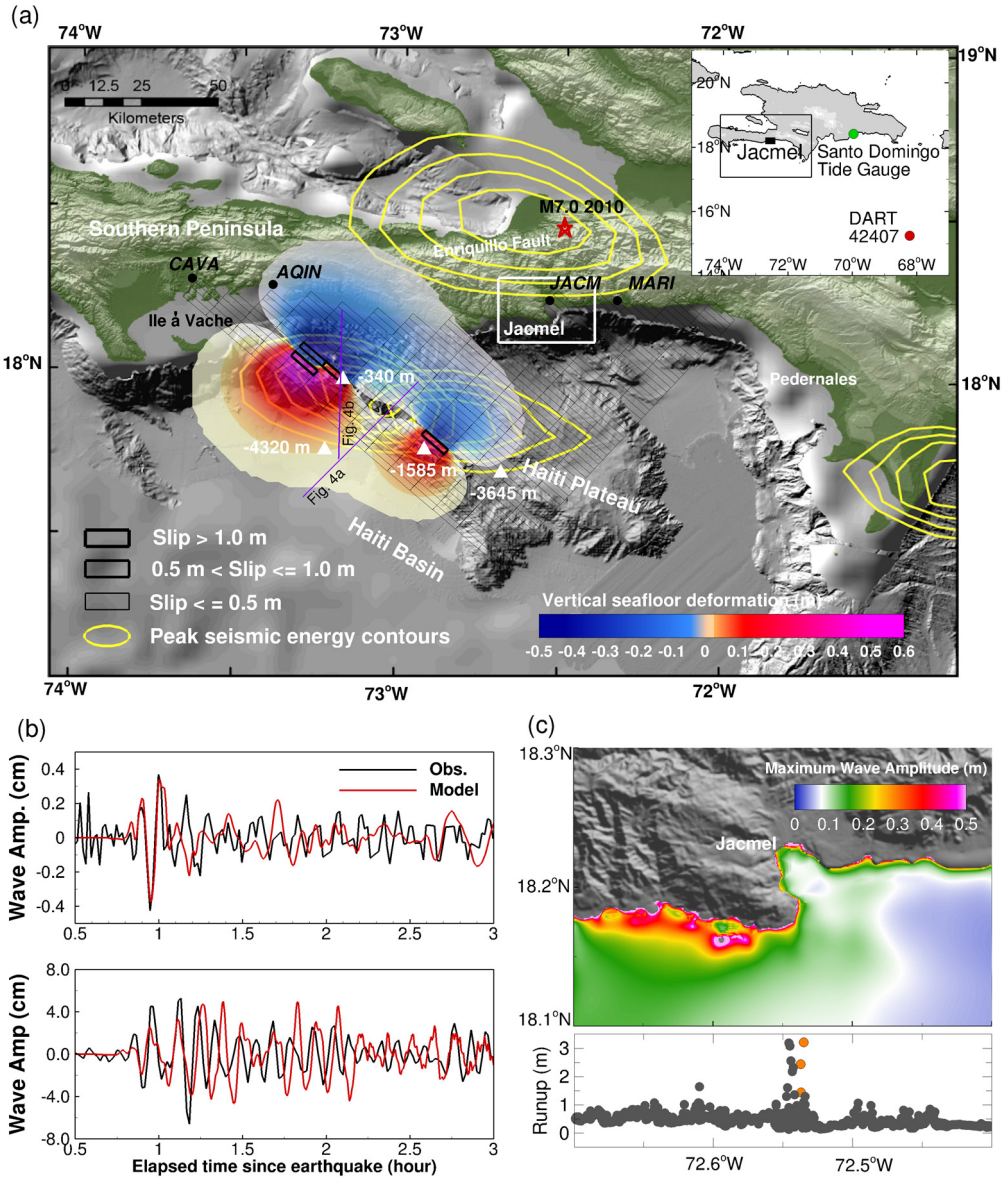

Fig. 1. Finite-fault model with strike of 132° and dip of 84°. Models with other strikes and dips are shown in Fig. 3 and in the Appendix. (*a*) Grid of rectangular elements - Finite-fault model configuration. Line thickness denotes modeled slip amplitude. See Table S1 for coordinates and slip of the finite faults. Downdip width of all sub-faults is 20 km and their top depth is 1 km. Colors denote vertical seafloor deformation from the tsunami source model calculated using Okada's (1985) analytical functions for an elastic half space. Yellow contours – Peak back-projected energy contours of the main shock and the three early aftershocks with values increasing inward from 60% to 90% (Fan and Shearer, 2016). Background – Shaded topography and bathymetry with selected elevations marked by white triangles. Topography is from SRTM 90 m grid. Shaded relief bathymetry is multibeam bathymetry compilation from various surveys gridded at 250 m and GEBCO grid. Red star – Epicenter of the 2010 Haiti earthquake. Purple lines – Seismic profiles shown in Fig. 4. Black dots – Campaign GPS sites. White rectangle – Location of map in (*c*). Inset: Locations of DART buoy and the Santo Domingo tide gauge station. (*b*) modeled and observed tsunami wave amplitudes at the DART buoy (top) and the Santo Domingo Tide Gauge (bottom). The inversion aims to fit the first observed waves on the DART buoy. (*c*) Calculated wave amplitude in the vicinity of Jacmel Bay (top) and calculated (black) and observed (orange) runup along the shoreline plotted by shoreline longitude. (For interpretation of the colors in the figure(s), the reader is referred to the web version of this article.)

We conducted a systematic search for the tsunami source(s) by fitting the sea-surface elevation waveform recorded on Deep-Ocean Assessment and Reporting of Tsunami (DART) buoy 42407 located in the Caribbean basin south of Santo Domingo (Fig. 1), as well as the tsunami arrival time at the Santo Domingo tide gauge, and the observed tsunami runup at Jacmel. Our best-fit sources are collocated with a shallow submarine ridge complex, which was previously proposed to be tectonically active (Bien-Aime Momplaisir, 1986), and with independently located, near-instantaneous dynamically triggered aftershocks of the earthquake (Fan and Shearer, 2016).

Near-instantaneous dynamically triggered aftershocks have been identified in the near to intermediate field during or immediately after the main shock rupture (D'Amico et al., 2010; Nissen et al., 2016; Wang et al., 2016; Fan and Shearer, 2016). (The term aftershock is used here to denote events that follow the largest shock of the earthquake sequence within the adjacent region). These aftershocks are triggered by transient passing seismic waves, such as seismic surface waves (Gomberg et al., 2001). They differ from statically triggered aftershocks, which are caused by the permanently altered Coulomb stress state in the crust and which are often located within one fault length of the mainshock fault (e.g., Harris, 1998). Dynamically triggered aftershocks can be almost as large as the main shock, such as with the M 7.0-7.1 1997 Harnai, Pakistan earthquake with a M 6.8 aftershock 19 s later on a separate reverse fault 50 km away (Nissen et al., 2016). In contrast, statically

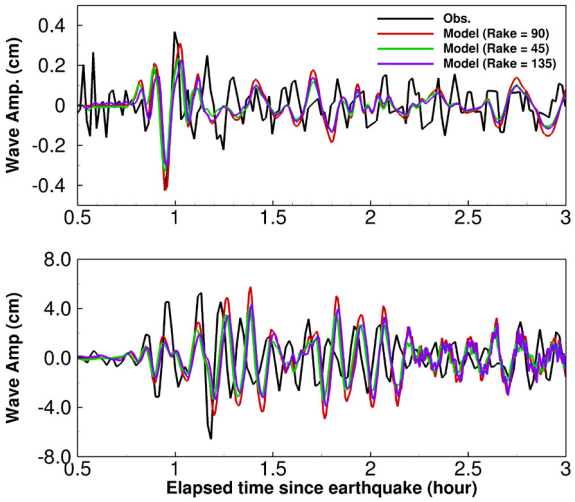

Fig. 2. Comparison of modeled tsunami wave amplitudes at the DART buoy (top) and the Santo Domingo Tide Gauge (bottom) for models with different rakes. All models have strike of 132° and dip of 84° similar to Fig. 1.

triggered aftershocks are often 1 to 1.2 magnitude units smaller than the main shock (e.g., Shearer, 2012). In either case, triggered aftershocks can rupture faults that are structurally disconnected from the main shock and can have varying focal mechanisms. Tsunami hazard assessments qualitatively consider rupturing splay faults and landslides triggered by the main shock as possible contributions to increased tsunami amplitude from subduction zone earthquakes (e.g., Moore et al., 2007; Fryer et al., 2004; Whitmore et al., 2008; Wendt et al., 2009; Fan et al., 2017). Our findings suggest that dynamically triggered early offshore aftershocks, such as those triggered by events on the San Andreas Fault, should also be considered in tsunami hazard assessments for large earthquakes on shore.

2. Analysis

We search for earthquake finite-fault sources that can explain the observed tsunami in the Caribbean Sea by inverting for slip on a set of reverse sub-faults within an area of 160 by ~100 km south of Haiti. Each sub-fault is 10 km along strike and 20 km down dip and its upper end is at a depth of 1 km. Because only one DART buoy exists in the Caribbean Sea, the analysis can only narrow down the range of permissible model parameters, rather than establish formal uncertainties. Additional criteria discussed below are used to further limit the model parameters. Following Wei et al. (2003), our inversion algorithm minimizes the misfit (in a least-squares sense) between the observed tsunami at DART buoy 42407 and the synthetic hydrodynamic wave at the buoy location from a linear combination of the sub-faults (Fig. 1). For the finite-fault model, each group of sub-faults can have any combination of strike (from a family of 117°, 132°, or 147°) and dip (84°, 60°, 45°, 30° or 15°) giving a total of 15 total possible geometries. The rake in each model is 90° (reverse faulting). Mixed reverse and strike-slip faulting, while possible, results in lower wave amplitudes for similar magnitude earthquake (Fig. 2). Given the plausible assumption that the unknown earthquake(s) had a smaller magnitude than the Haiti main shock, a 90° rake results in the largest tsunami wave. The possible sub-fault geometries are also guided by the focal mechanism of the 1997 M5.4 earthquake in the area, which was a reverse faulting earthquake with one nodal plane with strike 132°, dip 84° and rake of 95° (https://earthquake.usgs.gov/earthquakes/eventpage/usp0007vma#moment-tensor). The inversion algorithm attempted to fit the first two large peaks in the DART buoy record and a 2-hour long record. The initial finite-fault model is homogeneous with 1 m slip on each sub-fault. The inversion procedure assimilates the observed tsunami waveforms and gradually adjusts the slip at each sub-fault, rendering most of them zero slip. Table S1 lists the geographical coordinates and slip amount for each sub-fault with slip > 0 for each model.

We used the MOST (Method of Splitting Tsunami) model (Titov and Synolakis, 1995, 1998) for tsunami simulations. MOST solves the nonlinear depth-integrated shallow water equations, which are derived from the Navier-Stokes equations with the assumptions that 1) the tsunami waves propagate in an incompressible and irrotational medium; 2) tsunami propagation is primarily dominated by the geometry of the ocean floor; and 3) tsunami waves have much greater horizontal length scale than vertical length scale. MOST is capable of simulating tsunami generation, transoceanic propagation, and inundation and is the standard model used at the NOAA Center for Tsunami Research. The MOST model has been numerically verified against laboratory experimental results and benchmarks (Synolakis et al., 2008) and further validated with modern tsunamis simulated both after the fact and in real time (Tang et al., 2016; Wei et al., 2013; Tang et al., 2012; Wei et al., 2008). MOST uses the Manning's coefficient to account for the frictional resistance that the tsunami flow experiences when passing over the earth surface. A uniform Manning's coefficient of 0.03 is used in the inundation models along the coasts of Santo Domingo and Jacmel. MOST does not include the horizontal displacement effect on tsunami generation due to steep bathymetric features. However, an advantage of the DART-inverted source is that it accounts for the total energy built in the tsunami generation, no matter whether the source was horizontal or vertical. The preferred very steep dip in many of the inversions detailed in this paper could represent a bathymetric effect. MOST employs three variable resolution, telescoping grids to achieve increasing resolution of nearshore bathymetry starting with spatial resolution of 1 arc min (~1.8 km) and temporal step of 6 sec using the GEBCO 30 arc-sec global terrain model (https://www.gebco.net/data_and_products/gridded_bathymetry_data/gebco_30_second_grid/). The MOST inundation computation for the Haiti tsunami consisted of three telescoped grids with increasing spatial resolutions culminating in a spatial resolution of 3 arcsecond (~90 m). These 3 arcsecond grids were obtained from Caribbean 9-arcsecond bathymetric DEM developed by the NOAA Center for Tsunami Research, from a nautical chart of Jacmel Bay, and from the 3 arcsecond global Shuttle Radar Topography Mission (SRTM) (Farr et al., 2007). Note however, that the innermost grid, the 3 arcsecond grid, is based on sparse bathymetry of the nearshore region, limiting the accuracy of the simulations in the near shore.

3. Results

A suite of finite-fault models can explain the wavelength and amplitude of the first two peaks on the DART buoy (Figs. 1, 3, Supplementary figures S1–S10) and the first peak-trough transition in the Santo Domingo tide gauge data. (The later part of the tide gauge wavelet was not considered because of harbor oscillations). Our results suggest that the DART buoy data cannot constrain the finite-fault model uniquely. Models that fit the tsunami wave data equally well are shown in Figs. 1, 3 and in the Figs. S1, S2, S9, and S10 and include finite faults with strikes of 117°, 132°, 147° and dip of 84° and finite faults with strike of 117° and dips 30° and 15°. These seismic sources are located in the Caribbean Sea offshore the Southern Peninsula of Haiti.

As no previous seismological studies indicated any large seismic sources south of Haiti, we prefer finite-fault models with the smallest magnitude (Table 1). Such sources might have been buried in the 2010 Haiti earthquake mainshock coda and can be diffi-

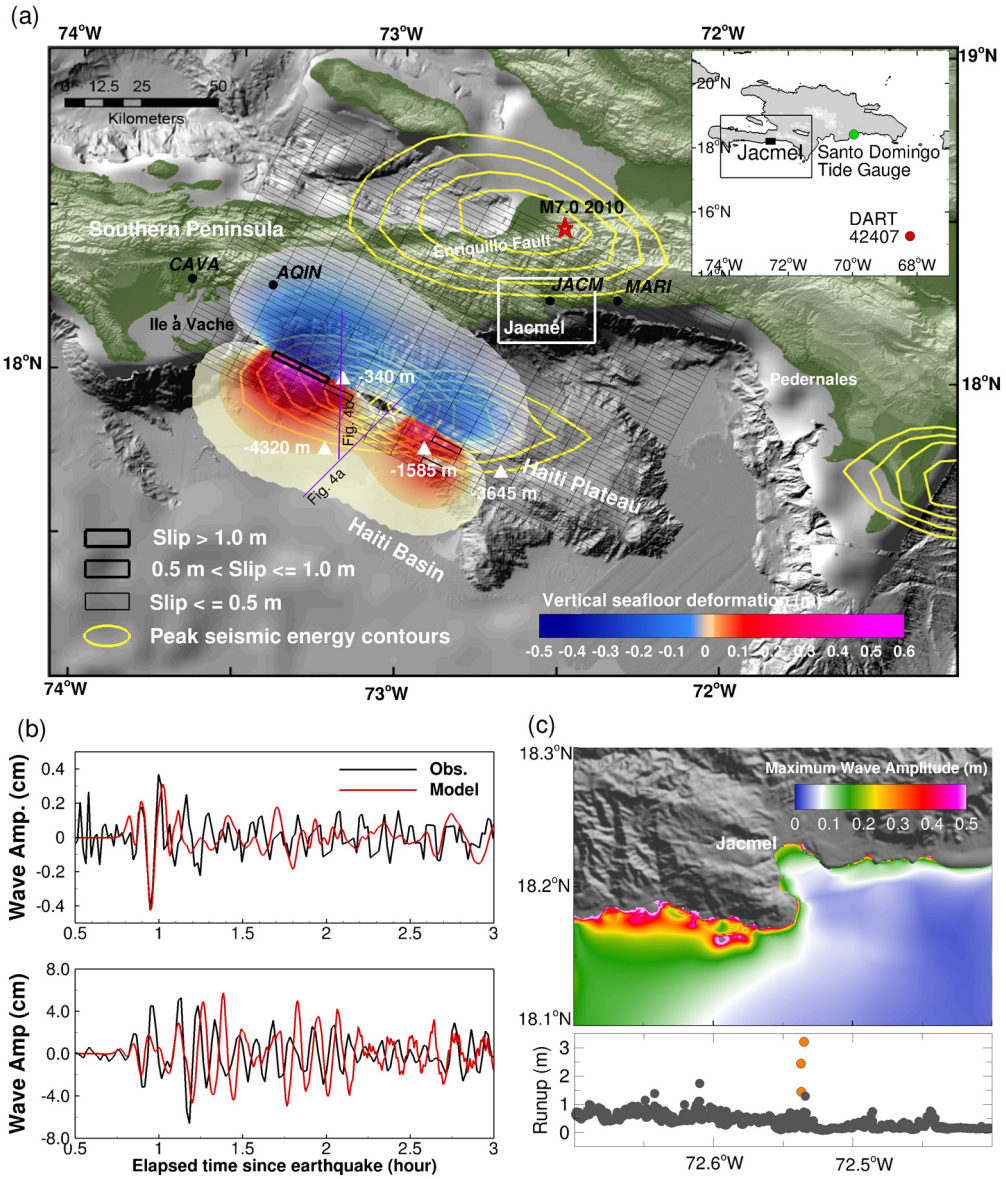

Fig. 3. Same as Fig. 1 but for a finite-fault model with a strike of 117° and a dip of 84° and an alternative inversion result (Inversion 2).

cult to resolve. We further prefer the smallest number of fault sources as expressed by the smallest number of sub-fault clusters. The vertical seafloor deformation generated by seismic sources with a dip of 84°and strikes of 117° (Inv. 2), 132° and 147°, as well as a source with strikes of 117° and 132° and a dip of 60°, have the smallest number (2–3) of source clusters (Table 1). These finite-fault sources form two aligned regions of uplift and subsidence (Figs. 1, 3, S2, S4). In all the models, the larger seafloor deformation is to the NW, with smaller deformation to the SE. Other models which fit the DART buoy data exhibit less contiguous sources and a more complex seafloor deformation map (Fig. S1, S5, S7–S12).

We can further narrow down the choice of models by examining the locations of these sources relative to the bathymetry (Table 1). Our preferred finite-fault models with strikes of 117° and 132° and dips of 84° and 60° (Figs. 1, 3, S3, and S4) align well with a ridge complex, which is indicated by a steep bathymetric variation extending southeast from Ile á Vache (Figs. 1, 4). The largest of the two finite-fault sources collocates with the shallowest submarine peak of this ridge (−340 m), and the smaller source collocates with a second submarine peak (−1585 m).

Bien-Aime Momplaisir (1986) hypothesized that the ridge extending from Ile á Vache may be undergoing compressional deformation. Re-processed seismic profiles HA82-3 from the 1982 Geophysical Services Incorporated survey and EW9501-1322 from the 1995 R/V Ewing multichannel seismic survey EW9501 show reverse faults cutting through the sea floor at the northeast flank of the ridge (Fig. 4). The ridge complex separates the 4300-m-deep Haiti sub-basin from an elevated seafloor to the NE, which is sometimes referred to as the Haiti Plateau (Fig. 1). The termination of basin stratigraphy against the ridge (Fig. 4) indicates, however, that the deformation is not focused at the basin-ridge boundary.

The amplitude of tsunami runup in Jacmel can be fit by finite-fault models with a strike of 132° and a dip of 84° (Fig. 1) and with a strike of 147° and a dip of 60° (Figs. S5). Both models generate a wave amplitude >3 m, similar to observations. However, only the model with a strike of 132° and a dip of 84° also fits the other criteria discussed above (Table 1).

The predicted magnitudes of the finite-fault model that best-fits the tsunami DART buoy waveform, the travel time to the Santo Domingo tide gauge and the observed runup at Jacmel (strike of 132° and a dip of 84°) are 6.83 for the major source in the

Table 1
Predicted magnitudes and subjective ranking of goodness of fit of the different finite-fault models to observations (1 is best fit).

Model Strike	Dip	Mw of two largest sources		Total Mw	Fit to first 2 waves	Fit to S.D. tide	Source clusters	Fit to ridge bathymetry in Jacmel	Fit to tsunami	Fit with aftershock locations	Fit to GPS	Sum
117 (inv1)	84	6.77	6.53	6.88	1	1	4	3	3	2	4	18
117 (inv2)	84	6.77	6.57	6.88	1	1	2	1	2	2	4	13
132	**84**	**6.83**	**6.45**	**6.90**	**1**	**1**	**2**	**1**	**1**	**1**	**2**	**9**
147	84	6.88	6.10	6.94	1	1	1	3	4	2	1	13
117	60	6.65	6.35	6.73	2	3	2	1	3	2	2	15
132	60	6.65	5.98	6.72	2	1	1	2	4	2	1	13
147	60	6.65	6.38	6.78	2	2	3	4	1	4	1	17
117	45	6.57	6.30	6.67	3	4	3	4	4	4	-	>22
132	45	6.84	6.25	6.91	2	3	3	4	4	3	-	>19
147	45	6.55	6.45	6.75	3	4	4	4	2	4	-	>21
117	30	7.16	6.71	7.20	1	1	4	4	4	4	-	>18
132*	30	-	-	7.40	-	-	-	-	-	-	-	-
147*	30	-	-	7.40	-	-	-	-	-	-	-	-
117	15	6.97	6.25	6.99	1	1	2	4	3	2	-	>13
132*	15	-	-	7.32	-	-	-	-	-	-	-	-

*Not ranked because total predicted magnitude was much larger than the magnitude of the main shock.
– Rigidity of 3×10^{10} N/m^2 is used for magnitude calculations.
– Qualitative ranking of finite-fault tsunami source clusters (simple source geometry) is represented by the number of non-contiguous sub-faults (rank 1–2 sub-fault clusters; rank 2–3 clusters; rank 4–5 or more clusters).
– Qualitative ranking of the collocation of tsunami sources with Ile á Vache ridge (rank 1 – all sub-faults are on the ridge; rank 2–1 sub-fault is not on the ridge; rank 4–3 or more sub-faults are not on the ridge).
– Qualitative ranking of tsunami observations in Jacmel: Rank 1 – wave amplitude >3 m; rank 2 – 2–3 m; rank 3 – 1–2 m; rank 4 – wave amplitude < 1.
– Qualitative ranking of tsunami source collocation with aftershock locations (rank 1 – all sub-faults are within the peak seismic energy contours; rank 2–1 sub-fault is outside the contours; rank 4–3 or more sub-faults are outside the contours).
– See Table 2 notes for explanation about the qualitative ranking of GPS fit.

northwest and 6.45 for the minor source in the southeast. The finite fault model is composed of two sources that are collocated with bathymetric peaks in a possibly tectonically active submarine ridge. The total energy release of our preferred finite-fault sources is 14% of the energy release from the tsunami source model proposed in Fritz et al. (2013). The predicted tsunami wave and tsunami runup from the best-fit finite-fault model, is similar to a model which also includes rupture of the main shock (compare Fig. 5 with Fig. 1). In other words, the 2010 Haiti main shock by itself could not have generated the observed tsunami in the Caribbean Sea.

4. Discussion

4.1. Supporting evidence

The predicted magnitudes of the finite-fault model that best-fit the tsunami observations (strike of 132° and a dip of 84°) is 6.83 for the major source in the northwest and 6.45 for the minor source in the southeast (Table 1, Fig. 1). The sub-faults that generate this model collocate well with the peak seismic energy of the early (20-60 s) aftershocks that were dynamically triggered by the Haiti earthquake. Several other models (Fig. 3, supplementary Figs. S1, S2, S3, S4, and S10) collocate almost as well with the early aftershocks. Three aftershocks hidden in the coda of the 2010 Mw 7.0 Haiti earthquake occurred 20–40 s, 40–60 s, and 120–140 s after the onset of the main shock (Fan and Shearer, 2016). These early aftershocks were detected by a back-projection method (Fan and Shearer, 2016), which takes advantage of the coherent phases recorded by globally distributed dense seismic arrays (Ishii et al., 2005; Kiser and Ishii, 2013). Such early aftershocks are dynamically triggered by large earthquakes ($7 \leq$ Mw < 8) within a few fault lengths (~300 km), when high-amplitude surface waves arrive from the mainshock (≤200 s).

To further understand the detected early aftershocks from back-projection, we evaluated the near-field dynamic peak strain field following the approach proposed by Pollitz et al. (2012). The source-time function for the 2010 Haiti earthquake was obtained from the SCARDEC database (http://scardec.projects.sismo.ipgp.fr/). We first calculated the initial 500 s wavefield with the PREM model (Dziewonski and Anderson, 1981) and the Instseis method (Driel et al., 2015) from the six-component GCMT moment tensor solution instead of the double-couple solution to account for the earthquake source complexity (see details of the complexity in Hayes et al., 2010), on 3D grids with 5 km spacing (horizontally and vertically). We then calculated the six-component strain tensor of grids at 10 km depth using a second order finite difference scheme (10 km is the middle depth of the finite faults in the preferred tsunami model with a dip of 84°, downdip width of 20 km starting 1 km below the surface). The Instseis method uses pre-computed Green's functions from the AxiSEM method (Nissen-Meyer et al., 2014). Here the synthetic seismograms are calculated with the PREM velocity model up to 5 s. Assuming the regional medium is Poisson solid with a Vp = 6 km/s and a density of 2830 kg/m3, we compute the regional stress tensor from the dynamic strain tensor assuming the medium is isotropic. Finally, the dynamic strain as well as the dynamic Coulomb stress on the preferred fault orientation were computed at each time step for a given grid on the preferred fault orientation (strike 132°, dip 84°, rake 90°) (Pollitz et al., 2012). Our results show that the 2010 Haiti mainshock generated a high strain field (>2.5 and >2 microstrain, respectively) and high dynamic coulomb stresses (300 and 200 kPa, respectively) in the vicinity of the two detected aftershocks (Fig. 6), which also collocates with the two subevents of the tsunami finite-fault model. The results suggest that the two aftershocks were likely dynamically triggered by the mainshock, and the back-projection detected early aftershocks are likely to be the two subevents resolved from the tsunami wave data.

The detected early aftershocks are unlikely to be artifacts from water or depth phases. As discussed in Fan and Shearer (2016, 2017), depth phases do not bias the results very much when stacking time windows longer than 20 s. In addition, although water-phases are likely to occur when reverse faulting earthquakes in the ocean rupture to the trench (Yue et al., 2017; Fan and Shearer, 2018), the 2010 Haiti earthquake ruptured faults on land. Therefore, the earthquake was unlikely to generate prominent water phases. Furthermore, p-waves over a large azimuthal range do not have extended multiple ringing effects (Fig. 7). Instead, the p-

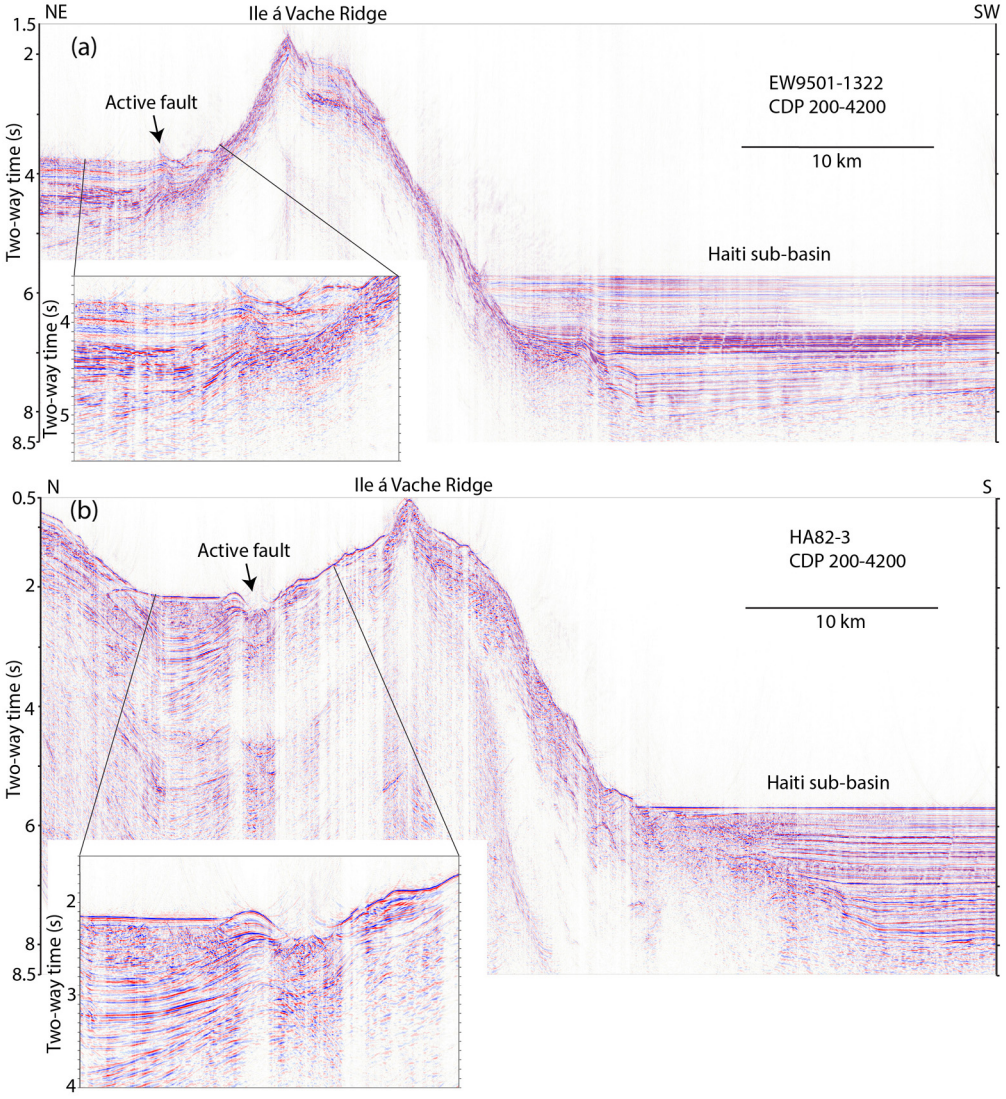

Fig. 4. Multichannel seismic profiles across Haiti sub-basin and Ile á Vache ridge complex. See Fig. 1 for their location. The structures in the two seismic lines are either a single curved ridge or two ridges with an along-strike relay or transfer zone between them. Note that the only active fault appears to be a sub-vertical reverse fault on the north side of the Ile á Vache ridge complex, not at the boundary between the ridge complex and Haiti sub-basin. Field data for profile EW9501-1322 was downloaded from the Academic Seismic Portal at LDEO http://www.marine-geo.org/portals/seismic/, and was stacked. Stacked profile HA82-3 is from Triezenberg et al. (2016). Both profiles were migrated using a 1500 m/s Stolt migration to remove noise due to seafloor diffractions.

waves associated with the early aftershocks show polarity reversals from 117° to 132° in azimuth confirming possible nodal planes of the focal-mechanism of the early aftershocks (Fig. 7).

Horizontal displacement due to rupture of several of the finite-fault models (strike of 147°) and dips of 84° and 60° in combination with the main shock, fit the observed co-seismic geodetic displacement at the campaign GPS sites AQIN, CAVA, JACM, and MARI along the south coast of the Southern Peninsula (Calais et al., 2010, Fig. 1) better than displacements from the main shock alone (Table 2). Other models, including our preferred model fit the observed co-seismic displacement almost as well as the main shock alone. All the models include the main shock solution from Calais et al. (2010) plus the finite-fault sources with slip >0.1 m (See supplementary Table S1 for source coordinates and slip). The surface horizontal displacement of the modeled sources was calculated using Coulomb 3.3 program (Lin and Stein, 2004; Toda et al., 2005).

We examined seismic records from stations within 15° of azimuthal distance from our modeled aftershocks for possible evidence of the aftershocks. Fig. 8 shows the predicted times of P, S, and surface waves of the main shock, and the predicted P and S arrivals of the aftershock for potential aftershocks occurring 30 and 130 s after the main shock at the preferred aftershock location (19.70°N, 73.12°W) Therefore, travel times from aftershock 30 and 130 s after the main shock bracket the arrival times of P and S waves from the proposed dynamic aftershocks. Note that with the exception of SDDR (Fig. 8d), P and S arrivals from an early aftershock 30 s occur within phases from the main shock, and hence cannot be distinguished with confidence (Fig. 8b). P arrivals from an aftershock 130 s can be observed on stations GRGR and BCIP (Fig. 8C) and may originate from the aftershock 120–140 s after the main shock. In summary, regional seismograms do not provide conclusive evidence for or against early aftershocks, in contrast to the back-projection method, which can distinguish sources by origin location using a dense array farther away.

It is not rare that arrivals from instantaneously triggered aftershocks can be missed by routine analyses due to high level of noise following the mainshock arrivals (e.g., Lay et al., 2010). Kiser and Ishii (2013) have shown that many of the aftershocks of the 2011 Tohoku earthquake were detected by the back-projection

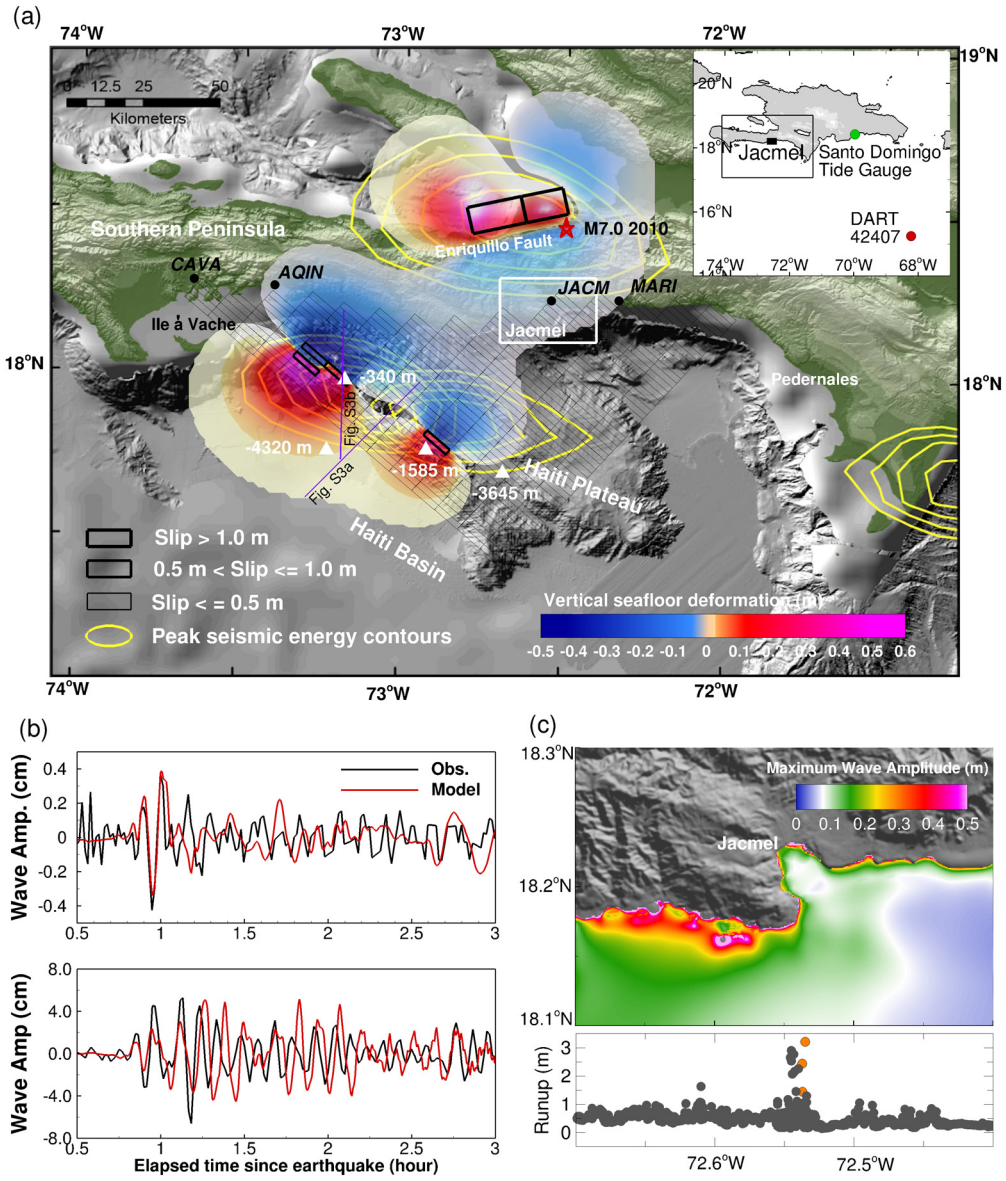

Fig. 5. Tsunami predictions from a model with both the main shock and the best-fitting finite fault model (strike 132° dip 84°). Comparison of the predictions of this model (*b*), (*c*) with those of Fig. 1 shows that the contribution of the main shock rupture to the tsunami in the Caribbean Sea is minor. See Fig. 1 for explanation of (*a*), (*b*), and (*c*). Main shock rupture parameters are from Calais et al. (2010).

Table 2
Comparison between observed co-seismic GPS displacements (in m) at four GPS sites along the south coast of Haiti's Southern Peninsula and calculated displacements from the main shock and the finite-fault models listed in Table S1.

	Observed	Main shock only	117_84_inv1	117_84_inv2	132_84	147_84	117_60	132_60	147_60
AQIN disp. (m)	0.016	0.010	0.040	0.048	0.027	0.008	0.023	0.008	0.014
CAVA disp. (m)	0.019	0.006	0.004	0.001	0.010	0.021	0.005	0.009	0.007
JACM disp. (m)	0.109	0.088	0.005	0.082	0.080	0.082	0.079	0.083	0.079
MARI disp. (m)	0.049	0.025	0.080	0.021	0.018	0.018	0.020	0.020	0.017
Δ disp. AQIN	–	0.400	1.502	2.035	0.676	0.510	0.453	0.495	0.150
Δ disp. CAVA	–	0.673	0.777	0.956	0.475	0.136	0.746	0.515	0.602
Δ disp. JACM	–	0.191	0.265	0.252	0.272	0.247	0.280	0.244	0.275
Δ disp. MARI	–	0.487	0.586	0.572	0.629	0.636	0.582	0.595	0.661
sum Δ disp.	–	1.751	3.130	3.815	2.053	1.529	2.061	1.849	1.689
Rank		1	4	4	2	1	2	1	1

1. Modeled sources are listed as strike and dip (e.g., 117_84 is strike 117 dip 84). Their coordinates are listed in Table S1.
2. The main shock rupture parameters are: −72.82° 18.413° to −72.446° 18.472°, dip – 60°, slip – 2.6 m left-lateral and 1.8 m reverse, top depth – 5 km, bottom depth – 15.5 km (Calais et al., 2010).
3. Δ disp is the absolute difference between observed and modeled displacement, normalized to the observed displacement = ABS[(observed-modeled)/observed] with 0 being a perfect fit.
4. Sum Δ displacement = ΔAQIN +ΔCAVA +ΔJACM +ΔMARI.
5. Qualitative ranking is based on sum Δ displacement: 1 – <2.0; 2 – 2.0–2.5; 3 – 2.5–3.0; 4 ≥3.0.

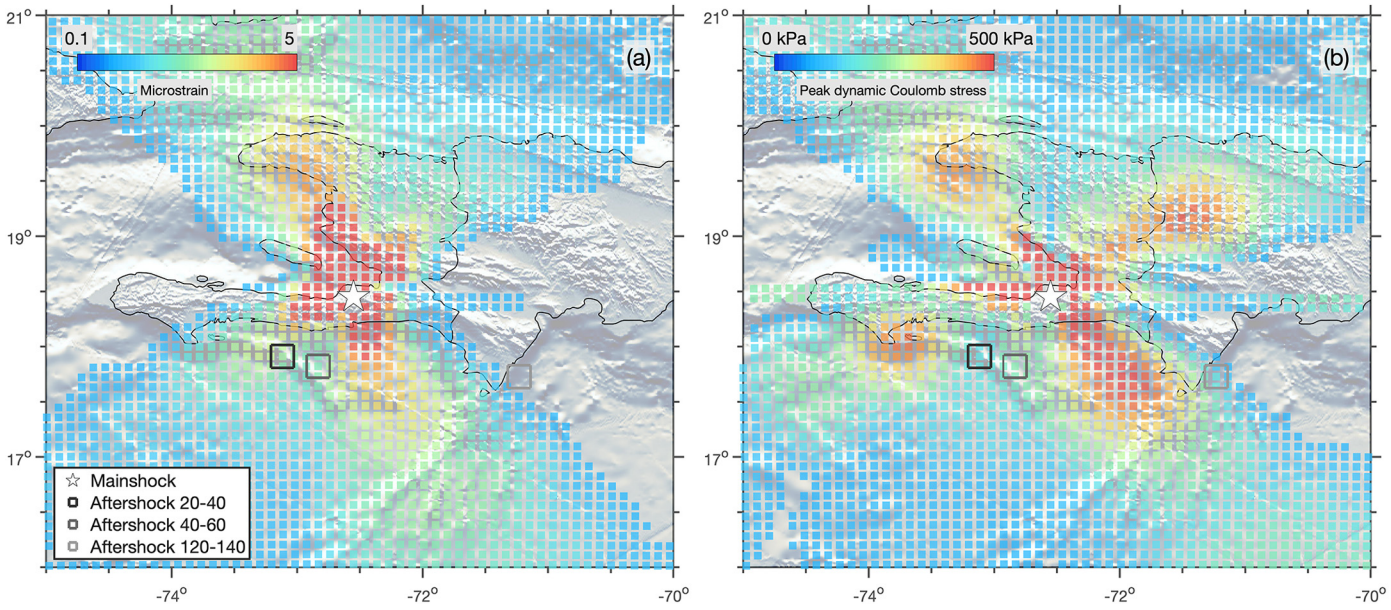

Fig. 6. Near-field peak second invariant dynamic strain due to the rupture of the main shock, calculated at a depth of 10 km. (b) Peak dynamic Coulomb stress on the preferred fault orientation (strike of 132, dip of 84, and rake of 90). See text for the computational details. A peak strain of ~2.5 microstrain and coulomb stress of 300 kPa is predicted in the location of first aftershock (20–40 s), which collocates with the largest assumed source of tsunami.

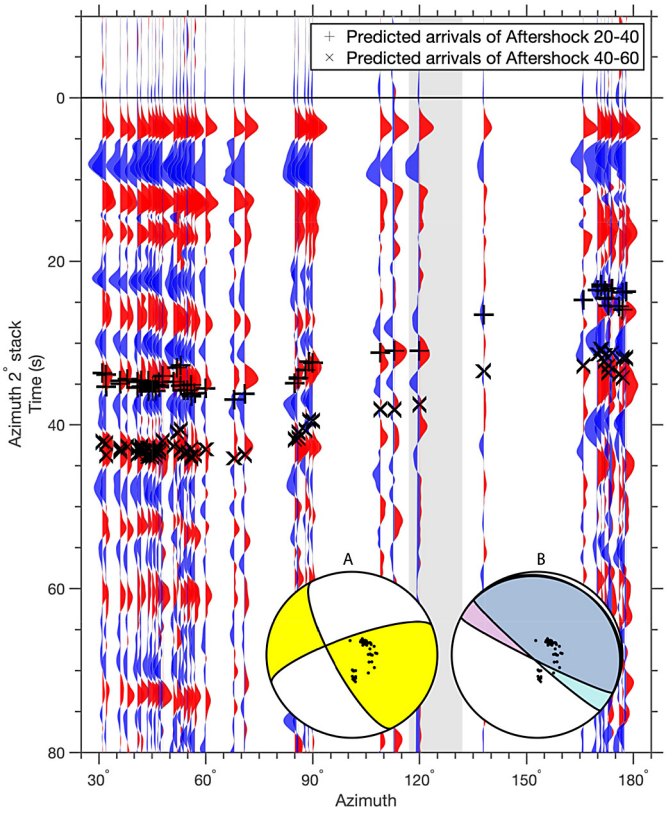

Fig. 7. Waveform alignment of the Haiti main shock recorded by the seismic global array. P-wave phases of the early aftershock do not show multiple ringing effects. The predicted arrivals from the early aftershocks coincide with coherent seismic phases. The grey band shows the likely strike ranges of the triggered early aftershocks. A polarity reversal occurred around this strike range, corresponding to a nodal plane striking at 123° of a possible focal-mechanism of the 20–40 s early aftershock (inset B). Inset A shows the mainshock double-couple focal mechanism.

method, but not by the dense Hi-net local seismic network. The largest event identified by the back-projection method and missed by the Japan Meteorological Agency (JMA) catalog had a magnitude of 6.8. The local Hi-net data showed only a very noisy arrival for this event and was difficult to identify in a high-pass filtered data (Kiser and Ishii, 2013). Kiser and Ishii (2013) hypothesized that the lack of detection in the JMA catalog may have been caused by a combination of the local velocity structure, differences in the rupture properties between the different earthquakes, and by increased background noise levels associated with the aftershock sequence. Another example is the 2016 M7 Kumamoto earthquake, which triggered a M5.8 earthquake ~80 km away. Only a handful of stations near the triggered event observed clear signals associated with the M5.8 earthquake, while most of the Hi-net stations, including some within a 50 km radius of the M5.8 event, missed the event (Uchide et al., 2016).

4.2. Other possible triggering sources

Poupardin et al. (2020) modeled the co-seismic displacement from four published finite-fault models for the 2010 Haiti earthquake. The displacement predicted by these four models only affected the north shore of the Southern Peninsula west of Port-au-Prince. Tsunami was indeed observed along the north shore with wave heights reaching 3 m in the vicinity of the earthquake epicenter causing 3 fatalities (Hornbach et al., 2010; Fritz et al., 2013). Slope failures of river deltas likely contributed to this tsunami. Fritz et al. (2013) proposed a finite-fault model to fit the observed tsunami in the Caribbean Sea. As discussed in the Introduction, their finite-fault model is not supported by geophysical observations and predicts significantly larger earthquake magnitude. Their waveform fit to the DART buoy and the SD tide station is also significantly worse than our best-fit models.

Subaerial and submarine landslides have been documented or suggested as tsunami sources (e.g. Okal and Synolakis, 2001; Fritz et al., 2007, Heiderzadeh et al., 2018). Small landslides and rock falls occurred along the southern coast of the peninsula both east and west of Jacmel (Harp et al., 2013; Fig. S11), but their contribution to a potential tsunami is unclear. A large (2 km^3) deep (3500 m) landslide scar ~30 km south of Jacmel was recently suggested to be the source of the tsunami in the Caribbean, but there is no evidence that it was triggered during the 2010 earthquake (Poupardin et al., 2020). In fact, submarine landslide scars can be

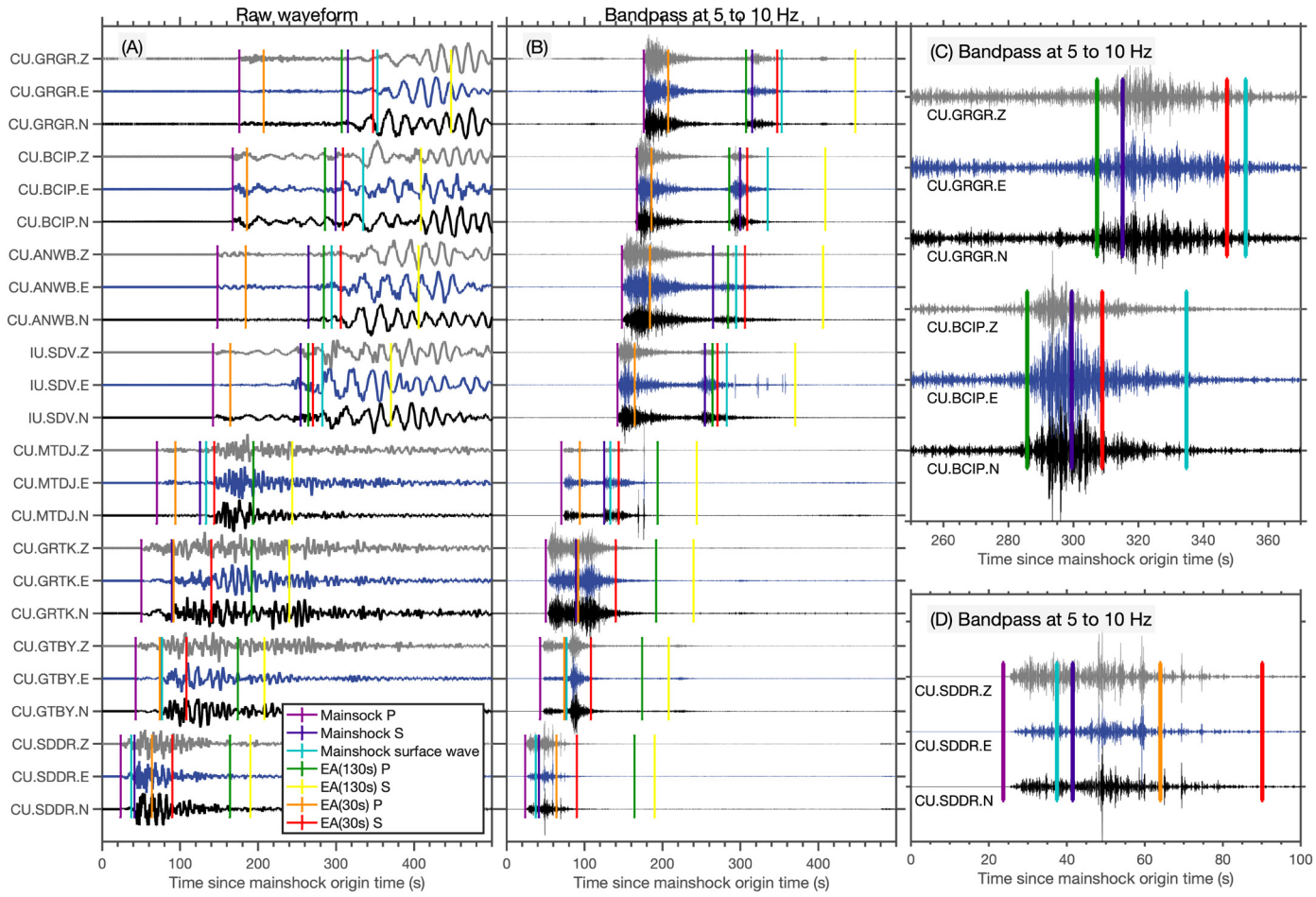

Fig. 8. Three-component seismograms around the time of the 2010 Haiti earthquake from seismic regional stations located less than 15° distance from the proposed aftershocks. (*a*) Raw waveforms; (*b*) waveforms filtered between 5–10 Hz. (*c*) Enlarged waveforms for stations GRGR and BCIP for the time interval of 250–370 s. (*d*) Enlarged waveforms for station SDDR for the time interval of 0–100 s. Colored lines are predicted, S, and surface wave arrivals of the main shock and P and S arrivals from aftershocks 30 and 130 s after the main shock calculated with the PREM model and surface wave velocity is assumed as 3.9 km/s. The 30 and 130 s aftershocks are located at the aftershock 20–40 s in Fig. 1.

preserved for thousands of years (e.g., Urlaub et al., 2013; ten Brink et al., 2014). Although the modeled travel-time from this slide approximates the observed times at the DART buoy and the SD tide station, the frequency of the modeled wavelet is double that recorded on the DART Buoy. The modeled high frequency is due to frequency dispersion of landslide sources (Fig. 10 in Poupardin et al., 2020). In addition, the fit of the travel times and amplitudes of the modeled landslide wavelet to the observed wavelet is much worse than the fit from earthquake sources shown in Fig. 1 and 3.

4.3. Implications

The collocation of the two subevents of the finite-fault model inferred from tsunami waves with the early aftershock locations and with a region of increased dynamic strain and the coincidence with a possible nodal plane for the aftershock with a strike of ~123° argue for a complex excitation mechanism for the observed Caribbean Sea tsunami. We propose that the propagating seismic waves from the 2010 Haiti earthquake dynamically triggered two early aftershocks on a tectonically active ridge within 60 s of the main shock, and the two early aftershocks then excited the observed tsunami at the DART buoy, at the tide gauge, and along the SE Haitian coast. The total energy needed to generate the observed tsunami is 1/7 of the energy release of the source model proposed in Fritz et al. (2013). The two aftershocks could either represent two ruptures or were part of the same rupture propagating from NW to SE along the submarine ridge (Fig. 1). These dynamically triggered aftershocks may be part of the active shortening across the Southern Peninsula (Wessels et al., 2019), which helps accommodate the NE-SW compression between the Caribbean and North American plates (e.g., Calais et al., 2010).

Earthquakes with onshore epicenters rarely trigger tsunamis. Therefore, it is peculiar that the 2010 Haiti earthquake caused a tsunami in the Caribbean Sea, even though it was ~27 km north of Hispaniola's Caribbean shoreline. In general, strike-slip earthquakes are also not expected to cause significant tsunamis because they are less effective at producing vertical seafloor motions. However, at least five strike-slip events between 1977–2004 were reported to have generated tsunamis (Whitmore et al., 2008). Geist and Parsons (2005) analyzed tsunamis caused by thrust aftershocks of the 2000 M8 New Ireland strike-slip earthquake and drew attention to the potential of large strike-slip faults such as the Alpine, Northern Anatolia and San Andreas faults to generate tsunamis. The 2018 Palu earthquake in Indonesia was a strike-slip earthquake and generated a prominent tsunami (Heiderzadeh et al., 2018). The 2010 Haiti ruptured along the onshore Enriquillo-Plantain Garden fault, one of the two main strike-slip fault systems accommodating the lateral motion between the North America and Caribbean plates. The collection of observations here suggests that land-based and strike-slip earthquake ruptures can cause tsunamis by dynamically triggering large aftershocks offshore and should, therefore, be incorporated into tsunami warning protocols.

5. Conclusions

We propose that early aftershocks hidden within the coda of the 2010 Haiti earthquake caused the enigmatic tsunami that was recorded on a DART buoy in the Caribbean Sea and a tide gauge at Santo Domingo harbor and that flooded Haiti's southern shore. We show that the main shock energy and configuration could not generate the tsunami by itself. Our best-fit aftershock sources of the tsunami had magnitudes of 6.8 and 6.5 and reverse-fault mechanisms and were located under a shallow possibly active submarine ridge south of Haiti ~85 km SW of the main shock epicenter. Back projection analysis of the seismic waves at teleseismic distances and the polarity of the arrivals buttress this interpretation, and calculation of the dynamic strain from the main shock suggest that the aftershocks were dynamically triggered. This example highlights the need to account for dynamically triggered aftershocks from land-based and strike-slip earthquake ruptures in tsunami warning protocols.

Declaration of competing interest

The authors declare that they have no known competing financial interests or personal relationships that could have appeared to influence the work reported in this paper.

Acknowledgements

We thank Dave Foster for help with processing the seismic profiles. Earlier reviews by Eric Geist, Diego Arcas, and Aditya Gusman, are gratefully acknowledged. DART buoy data is available from the National Data Buoy Center (http://www.ndbc.noaa.gov/dart.shtml), and the tide gauge data is available from the Sea Level Station Monitoring Facility of the Intergovernmental Oceanographic Commission of UNESCO (http://www.ioc-sealevelmonitoring.org). Yong Wei's work is funded by the Joint Institute for the Study of the Atmosphere and Ocean (JISAO) under NOAA Cooperative Agreement NA15OAR4320063, Contribution No. 2017-0123, PMEL Contribution No. 4731 and by the USGS Coastal and Marine Hazards and Resources Program. José Luis Granja-Bruña was partially funded by the Spanish research project CGL2010-17715.

Appendix A. Supplementary material

Supplementary material related to this article can be found online at https://doi.org/10.1016/j.epsl.2020.116269.

References

Bien-Aime Momplaisir, R., 1986. Contribution à l'étude géologique de la partie orientale du massif de la Hotte, Presqu'île du sud d'Haïti. Synthèse structurale des marges de la Presqu'île à partir de données sismiques. Thése. De l'Université Paris 6. 223 pp.

Calais, E., Freed, A., Mattioli, G., Amelung, F., Jónsson, S., Jansma, P., Hong, S.H., Dixon, T., Prépetit, C., Momplaisir, R., 2010. Transpressional rupture of an unmapped fault during the 2010 Haiti earthquake. Nat. Geosci. 3, 794.

D'Amico, S., Koper, K.D., Herrmann, R.B., Akinci, A., Malagnini, L., 2010. Imaging the rupture of the Mw 6.3 April 6, 2009 L'Aquila, Italy earthquake using back-projection of teleseismic P-waves. Geophys. Res. Lett. 37 (3).

Douilly, R., Haase, J.S., Ellsworth, W.L., Bouin, M.P., Calais, E., Symithe, S.J., Armbruster, J.G., de Lépinay, B.M., Deschamps, A., Mildor, S.L., Meremonte, M.E., 2013. Crustal structure and fault geometry of the 2010 Haiti earthquake from temporary seismometer deployments. Bull. Seismol. Soc. Am. 103, 2305–2325.

Driel, M.v., Krischer, L., Stähler, S.C., Hosseini, K., Nissen-Meyer, T., 2015. Instaseis: instant global seismograms based on a broadband waveform database. Solid Earth, 701–717.

Dziewonski, A.M., Anderson, D.L., 1981. Preliminary reference Earth model. Phys. Earth Planet. Inter. 25, 297–356.

Fan, W., Shearer, P.M., 2017. Investigation of backprojection uncertainties with M6 earthquakes. J. Geophys. Res., Solid Earth 122, 7966–7986.

Fan, W., Shearer, P.M., 2016. Local near instantaneously dynamically triggered aftershocks of large earthquakes. Science 353, 1133–1136.

Fan, W., Shearer, P.M., 2018. Coherent seismic arrivals in the p wave coda of the 2012 Mw 7.2 Sumatra earthquake: water reverberations or an early aftershock? J. Geophys. Res., Solid Earth 123, 3147–3159.

Fan, W., Bassett, D., Jiang, J., Shearer, P.M., Ji, C., 2017. Rupture evolution of the 2006 Java tsunami earthquake and the possible role of splay faults. Tectonophysics 721, 143–150.

Farr, T.G., Rosen, P.A., Caro, E., Crippen, R., Duren, R., Hensley, S., Kobrick, M., Paller, M., Rodriguez, E., Roth, L., Seal, D., Shaffer, S., Shimada, J., Umland, J., Werner, M., Oski, M., Burbank, D., Alsdorf, D., 2007. The shuttle radar topography mission. Rev. Geophys. 45, RG2004. https://doi.org/10.1029/2005RG000183.

Fritz, H.M., Kongko, W., Moore, A., McAdoo, B., Goff, J., Harbitz, C., Uslu, B., Kalligeris, N., Suteja, D., Kalsum, K., Titov, V., 2007. Java tsunami. Geophys. Res. Lett. 34 (12). Extreme runup from the 17 July 2006.

Fritz, H.M., Hillaire, J.V., Molière, E., Wei, Y., Mohammed, F., 2013. Twin tsunamis triggered by the 12 January 2010 Haiti earthquake. Pure Appl. Geophys. 170, 1463–1474.

Fryer, G.J., Watts, P., Pratson, L.F., 2004. Source of the great tsunami of 1 April 1946: a landslide in the upper Aleutian forearc. Mar. Geol. 203, 201–218.

Geist, E.L., Parsons, T., 2005. Triggering of tsunamigenic aftershocks from large strike-slip earthquakes: analysis of the November 2000 new Ireland earthquake sequence. Geochem. Geophys. Geosyst. 6 (10).

Gomberg, J., Reasenberg, P., Bodin, P., Harris, R., 2001. Earthquake triggering by seismic waves following the Landers and Hector Mine earthquakes. Nature 411, 462–466.

Harp, E.L., Jibson, R.W., Dart, R.L., 2013. The Effect of Complex Fault Rupture on the Distribution of Landslides Triggered by the 12 January 2010, Haiti Earthquake Landslide Science and Practice. Springer, pp. 157–161.

Harris, R.A., 1998. Introduction to special section: stress triggers, stress shadows, and implications for seismic hazard. J. Geophys. Res., Solid Earth 103, 24347–24358.

Hayes, G.P., Briggs, R.W., Sladen, A., Fielding, E.J., Prentice, C., Hudnut, K., Mann, P., Taylor, F.W., Crone, A.J., Gold, R., Ito, T., 2010. Complex rupture during the 12 January 2010 Haiti earthquake. Nat. Geosci. 3, 800–805.

Heiderzadeh, M., Muhari, A., Wijanarto, A.B., 2018. Insights on the source of the 28 September 2018 Sulawesi tsunami, Indonesia based on spectral analyses and numerical simulations. Pure Appl. Geophys. 1 (19).

Hornbach, M.J., Braudy, N., Briggs, R.W., Cormier, M.H., Davis, M.B., Diebold, J.B., Dieudonne, N., Douilly, R., Frohlich, C., Gulick, S.P., Johnson III, H.E., 2010. High tsunami frequency as a result of combined strike-slip faulting and coastal landslides. Nat. Geosci. 3 (11), 783–788.

Ishii, M., Shearer, P.M., Houston, H., Vidale, J.E., 2005. Extent, duration and speed of the 2004 Sumatra–Andaman earthquake imaged by the Hi-Net array. Nature 435, 933–936.

Kiser, E., Ishii, M., 2013. Hidden aftershocks of the 2011 Mw 9.0 Tohoku, Japan earthquake imaged with the backprojection method. J. Geophys. Res., Solid Earth 118 (10), 5564–5576.

Lay, T., Ammon, C.J., Kanamori, H., Rivera, L., Koper, K.D., Hutko, A.R., 2010. The 2009 Samoa–Tonga great earthquake triggered doublet. Nature 466 (7309), 964.

Lin, J., Stein, R.S., 2004. Stress triggering in thrust and subduction earthquakes, and stress interaction between the southern San Andreas and nearby thrust and strike-slip faults. J. Geophys. Res. 109, B02303. https://doi.org/10.1029/2003JB002607.

Moore, G., Bangs, N., Taira, A., Kuramoto, S., Pangborn, E., Tobin, H., 2007. Three-dimensional splay fault geometry and implications for tsunami generation. Science 318, 1128–1131.

Nissen-Meyer, T., Driel, M.V., Stähler, S., Hosseini, K., Hempel, S., Auer, L., Colombi, A., Fournier, A., 2014. AxiSEM: broadband 3-d seismic wavefields in axisymmetric media. Solid Earth, 425–445.

Nissen, E., Elliott, J.R., Sloan, R.A., Craig, T.J., Funning, G.J., Hutko, A., Parsons, B.E., Wright, T.J., 2016. Limitations of rupture forecasting exposed by instantaneously triggered earthquake doublet. Nat. Geosci. 9, 330–336.

Okada, Y., 1985. Surface deformation due to shear and tensile faults in a half-space. Bull. Seismol. Soc. Am. 75, 1135–1154.

Okal, E.A., Synolakis, C.E., 2001. Comment on "Origin of the 17 July 1998 Papua New Guinea tsunami: earthquake or landslide?" by E.L. Geist. Seismol. Res. Lett. 72 (3), 362–366.

Pollitz, F.F., Stein, R.S., Sevilgen, V., Bürgmann, R., 2012. The 11 April 2012 East Indian Ocean earthquake triggered large aftershocks worldwide. Nature 490, 250.

Poupardin, A., Calais, E., Heinrich, P., Hébert, H., rodriguez, M., Lery, S., Aochi, H., Douilly, R., 2020. Deep submarine landslide contribution to the 2010 Haiti earthquake tsunami. Natural Hazards Earth Syst. Sci. https://doi.org/10.5194/nhess-2019-388.

Shearer, P.M., 2012. Self-similar earthquake triggering, Båth's law, and foreshock/aftershock magnitudes: simulations, theory, and results for southern California. J. Geophys. Res., Solid Earth 117 (B6).

Symithe, S.J., Calais, E., Haase, J.S., Freed, A.M., Douilly, R., 2013. Coseismic slip distribution of the 2010 M 7.0 Haiti earthquake and resulting stress changes on regional faults. Bull. Seismol. Soc. Am. 103, 2326–2343.

Synolakis, C.E., Bernard, E.N., Titov, V.V., Kanoglu, U., Gonzalez, F.I., 2008. Validation and verification of tsunami numerical models. Pure Appl. Geophys. 165, 2197–2228.

Tang, L., Titov, V.V., Bernard, E.N., Wei, Y., Chamberlin, C., Newman, J.C., Mofjeld, H., Arcas, D., Eble, M., Moore, C., Uslu, B., Pells, C., Spillane, M.C., Wright, L.M., Gica, E., 2012. Direct energy estimation of the 2011 Japan tsunami using deep-ocean pressure measurements. J. Geophys. Res. 117, C08008. https://doi.org/10.1029/2011JC007635.

Tang, L., Titov, V.V., Moore, C., Wei, Y., 2016. Real-time assessment of the 16 September 2015 Chile tsunami and implications for near-field forecast. Pure Appl. Geophys. 173, 369–387. https://doi.org/10.1007/s00024-015-1226-3.

ten Brink, U.S., Chaytor, J.D., Geist, E.L., Brothers, D.S., Andrews, B.D., 2014. Assessment of tsunami hazard to the US Atlantic margin. Mar. Geol. 353, 31–54.

Titov, V.V., Synolakis, C.E., 1995. Modeling of breaking and nonbreaking long-wave evolution and runup using VTCS-2. J. Waterw. Port Coast. Ocean Eng. 121, 308–316.

Titov, V.V., Synolakis, C.E., 1998. Numerical modeling of tidal wave runup. J. Waterw. Port Coast. Ocean Eng. 124, 157–171.

Toda, S., Stein, R.S., Richards-Dinger, K., Bozkurt, S., 2005. Forecasting the evolution of seismicity in southern California: animations built on earthquake stress transfer. J. Geophys. Res. 110, B05S16. https://doi.org/10.1029/2004JB003415.

Triezenberg, P.J., Hart, P.E., Childs, J.R., 2016. National archive of marine seismic surveys, NAMSS: a USGS data website of marine seismic reflection data within the U.S. exclusive economic zone, EEZ: U.S. geological survey data release. https://doi.org/10.5066/F7930R7P.

Uchide, T., Horikawa, H., Nakai, M., Matsushita, R., Shigematsu, N., Ando, R., Imanishi, K., 2016. The 2016 Kumamoto–Oita earthquake sequence: aftershock seismicity gap and dynamic triggering in volcanic areas. Earth Planets Space 68, 180. https://doi.org/10.1186/s40623-016-0556-4.

Urlaub, M., Talling, P.J., Masson, D.G., 2013. Timing and frequency of large submarine landslides: implications for understanding triggers and future geohazard. Quat. Sci. Rev. 72, 63–82.

Wang, D., Mori, J., Koketsu, K., 2016. Fast rupture propagation for large strike-slip earthquakes. Earth Planet. Sci. Lett. 440, 115–126.

Wei, Y., Bernard, E.N., Tang, L., Weiss, R., Titov, V.V., Moore, C., Spillane, M., Hopkins, M., Kânoğlu, U., 2008. Real-time experimental forecast of the Peruvian tsunami of August 2007 for U.S. coastlines. Geophys. Res. Lett. 35, L04609. https://doi.org/10.1029/2007GL032250.

Wei, Y., Chamberlin, C., Titov, V.V., Tang, L., Bernard, E.N., 2013. Modeling of the 2011 Japan tsunami - lessons for near-field forecast. Pure Appl. Geophys. 170, 1309–1331. https://doi.org/10.1007/s00024-012-0519-z.

Wei, Y., Cheung, K.F., Curtis, G.D., McCreery, C.S., 2003. Inverse algorithm for tsunami forecasts. J. Waterw. Port Coast. Ocean Eng. 129, 60–69.

Wessels, R.J., Ellouz-Zimmermann, N., Bellahsen, N., Hamon, Y., Rosenberg, C., Deschamps, R., Momplaisir, R., Boisson, D., Leroy, S., 2019. Polyphase tectonic history of the Southern Peninsula, Haiti: from folding-and-thrusting to transpressive strike-slip. Tectonophysics 751, 125–149.

Wendt, J., Oglesby, D.D., Geist, E.L., 2009. Tsunamis and splay fault dynamics. Geophys. Res. Lett. 36 (15).

Whitmore, P., Benz, H., Bolton, M., Crawford, G., Dengler, L., Fryer, G., Malone, S., 2008. NOAA/West coast and Alaska tsunami warning center Pacific Ocean response criteria. Sci. Tsunami Hazards 27, 1–19.

Yue, H., Castellanos, J.C., Yu, C., Meng, L., Zhan, Z., 2017. Localized water reverberation phases and its impact on backprojection images. Geophys. Res. Lett. 44, 9573–9580.